

Restoration of chopped and noded images in infrared astronomy

This article has been downloaded from IOPscience. Please scroll down to see the full text article.

1999 Inverse Problems 15 345

(<http://iopscience.iop.org/0266-5611/15/2/002>)

View [the table of contents for this issue](#), or go to the [journal homepage](#) for more

Download details:

IP Address: 130.251.61.251

The article was downloaded on 21/04/2010 at 07:59

Please note that [terms and conditions apply](#).

Restoration of chopped and nodded images in infrared astronomy

M Bertero[†], P Boccacci[‡], F Di Benedetto[§] and M Robberto^{||}

[†] INFM and Dipartimento di Informatica e Scienze dell'Informazione, Università di Genova, Via Dodecaneso 35, Genova, Italy

[‡] INFM and Dipartimento di Fisica, Università di Genova, Via Dodecaneso 33, Genova, Italy

[§] Dipartimento di Matematica, Università di Genova, Via Dodecaneso 35, Genova, Italy

^{||} Max Planck Institut für Astronomie, Heidelberg, Germany and Osservatorio Astronomico di Torino, Italy

Received 18 September 1998

Abstract. In thermal infrared astronomy a differential technique is used for extracting the weak astronomical image from the large background due to the environment. The resulting images, the so-called chopped and nodded images, present large negative values and provide reliable representations uniquely in the case of isolated sources. In this paper we discuss the mathematical properties of the problem of restoring the original image from its chopped and nodded version and we investigate an iterative regularization method, the so-called projected Landweber method, for approximating non-negative solutions of the problem. This method provides satisfactory results in some cases but, in general, the restored images are still affected by several artifacts. We suggest an observation strategy which, combined with our proposed restoration method, can significantly reduce the effect of these artifacts.

1. Introduction

In thermal infrared astronomy ($\lambda \geq 2.4 \mu\text{m}$), the unknown brightness distribution of the celestial source f is normally superposed on a large and variable background a due to the thermal emission from the atmosphere and telescope optics. If x, y are angular coordinates in the sky, the signal s coming from the direction $\{x, y\}$ at time t and detected at a point P of the image plane is given by

$$s = f(x, y) + a(x, y, t). \quad (1)$$

It is clear that to extract $f(x, y)$ it is necessary to estimate $a(x, y, t)$. This could be done by pointing the telescope to a sky area close to the region of interest at a time t' close to t . Assuming that this area corresponds to a shift Δ in the y coordinate, then the new signal s_1 detected at the point P is

$$s_1 = f(x, y + \Delta) + a(x, y + \Delta, t'). \quad (2)$$

If the sky area close to that of interest is empty, i.e. $f(x, y + \Delta) = 0$, and close enough that the background is approximately the same, i.e. $a(x, y + \Delta, t') \simeq a(x, y, t)$, then by subtracting (2) from (1) one can obtain $f(x, y)$.

In practice, the telescope must be pointed repeatedly to the two sky areas and rapidly enough in time to avoid any significant variation of a . The actual time frequency of this operation depends on various factors, such as observing wavelength, weather conditions,

telescope location and so on, but must be typically of the order of a few hertz to compensate for the atmospheric fluctuations. It is, in general, impossible to repeatedly move a large telescope at these frequencies. However, a single element of the telescope optics can be rapidly modulated between two slightly different positions, allowing the detector to see two nearby sky areas. This technique is called *chopping* and the quantity Δ , therefore, is called the *chopping throw* or *chopping amplitude*.

This method, which is the one normally adopted, presents two major drawbacks. First, by moving an optical element of the system, the resulting differential image turns out to be affected by a residual background variation due to the thermal differences between the two telescope beams. In other words, to observe the source and the sky (almost) simultaneously is equivalent to using two different telescopes, one (*A*) for the source and another (*B*) for the sky. We will denote by Δa_{AB} the residual difference between the corresponding backgrounds.

Second, for optical and mechanical reasons it is not possible to observe sky areas too far from the original source position. Typical angular amplitudes for the chopping are less than 60 seconds of arc. If the source is extended enough, it can be that $f(x, y + \Delta) \neq 0$. Therefore, the subtraction of (2) from (1) gives

$$\Delta s_A = s - s_1 = f(x, y) - f(x, y + \Delta) + \Delta a_{AB} \quad (3)$$

where with Δs_A we indicate that the source has been observed with (*A*).

To remove the term Δa_{AB} , the so-called *beam-switching* or *nodding* technique is applied: the telescope is pointed to a different point on the sky, in such a way that the source will be observed with (*B*), i.e. the telescope is pointed to a region which is obtained by a shift $-\Delta$ in the *y* coordinate. In this way, at the point *P* the signal s_2 is obtained and, repeating the entire sequence, the result is

$$\Delta s_B = s_2 - s = f(x, y - \Delta) - f(x, y) + \Delta a_{AB}. \quad (4)$$

Subtracting (4) from (3), one gets the so-called *chopped and noded image*:

$$g(x, y) = \Delta s_A - \Delta s_B = -f(x, y - \Delta) + 2f(x, y) - f(x, y + \Delta) \quad (5)$$

i.e. an image which is independent of the atmospheric background and telescope thermal pattern. If the source brightness distribution is sufficiently compact, i.e. if $f(x, y - \Delta) = f(x, y + \Delta) = 0$, then the problem of extracting $f(x, y)$ is solved. In general, however, the image $g(x, y)$ must be inverted to recover the spatial brightness distribution of the source $f(x, y)$.

An inversion method for (5) is at present not available, but we foresee that soon it will be highly needed. The continuous technological developments both in the field of infrared array detectors, which now allow natural background-noise limited performances, and of large telescope engineering, with approximately a dozen 8 m class telescopes in operation or in an advanced construction phase, are greatly improving the sensitivity of thermal infrared instrumentation. Taking into account the fact that the size of panoramic detectors is rapidly increasing and that giant telescopes provide very small fields of view and limited angular amplitudes for the chopping, the case $f(x, y - \Delta) = f(x, y + \Delta) = 0$ can no longer be regarded as the standard case. In this paper we address the problem of inverting (5), i.e. the problem of recovering $f(x, y)$ from the measured values of $g(x, y)$.

By means of the Fourier transform we get from (5)

$$\hat{g}(\omega_x, \omega_y) = 4 \sin^2(\frac{1}{2} \Delta \omega_y) \hat{f}(\omega_x, \omega_y) \quad (6)$$

where ω_x, ω_y are the frequencies associated with the spatial variables *x, y*, respectively. As already observed by Beckers [1], equation (6) shows that the chopped and noded image does not contain information about $\hat{f}(\omega_x, \omega_y)$ at the spatial frequencies $\omega_{y,k} = 2\pi k/\Delta$

($k = 0, \pm 1, \pm 2, \dots$), even if the Fourier transform of the measured data is not zero at these frequencies because of the noise contaminating $g(x, y)$ [2]. As a consequence a restoration of $\hat{f}(\omega_x, \omega_y)$ cannot be obtained by dividing equation (6) with the factor $\sin^2(\Delta\omega_y/2)$: the problem of restoring $f(x, y)$ from $g(x, y)$ is a typical example of an ill-posed problem.

If we assume that $f(x, y)$ and $g(x, y)$ are sampled with a sampling distance δ (both in the x and in the y coordinates) and that $\Delta = K\delta$ with K integer, then (5) is replaced by the following discrete relationship

$$g_{j,m} = -f_{j,m-K} + 2f_{j,m} - f_{j,m+K} \quad (7)$$

where $g_{j,m}$ and $f_{j,n}$ are the samples of $g(x, y)$ and $f(x, y)$, respectively. In the following we will omit for simplicity the index j since the restoration procedure does not depend on the x variable when the chopping is in the y direction.

We consider a finite image which consists of N values g_m ($m = 1, 2, \dots, N$), forming the components of a vector \mathbf{g} of length N . According to (7) this vector receives contributions from $N + 2K$ values f_n which form the components of a vector \mathbf{f} of length $N + 2K$. If these components are indexed with $n = 1, 2, \dots, N + 2K$, then the relationship between the vectors \mathbf{f} and \mathbf{g} is given by

$$g_m = -f_m + 2f_{m+K} - f_{m+2K} \quad (8)$$

and the problem is that of restoring \mathbf{f} , given \mathbf{g} . The components of \mathbf{f} with n running from $K + 1$ up to $K + N$ correspond to the sampling points in the region of interest which will be called the *observation region*. We point out that, in general, it is more important to restore these components than the others and this point will be taken into account in the following.

The paper is organized as follows. In section 2 we derive several properties of the rectangular matrix relating the vectors \mathbf{f} and \mathbf{g} . In particular, we characterize its null space and singular system and we estimate its ill-conditioning. In section 3 we investigate the generalized solution of the restoration problem and we show, by means of numerical examples, that it does not provide a satisfactory solution of the problem. In section 4 we look for the non-negative solution with minimal Euclidean norm and we propose the projected Landweber method as a useful iterative method for approximating and regularizing this solution. The implementation and validation of the method by means of numerical examples is considered in section 5. Since the non-negative solution of minimal norm still exhibits artifacts which in some cases can be very large, a way to reduce them is proposed in section 6. It consists of using chopped and nodded images of the same source obtained with different chopping amplitudes and of averaging the corresponding restorations over the observation region. By means of simulations we show that this method can provide satisfactory results. Finally, in section 7 we summarize the conclusions of our work. Some mathematical details are reported in the appendices.

2. Properties of the imaging matrix

Equation (8) defines a matrix \mathbf{A} , with N rows and $N + 2K$ columns, which will be called the *imaging matrix*. It is given by

$$(\mathbf{A})_{m,n} = -\delta_{m,n} + 2\delta_{m+K,n} - \delta_{m+2K,n} \quad (9)$$

where $\delta_{m,n} = 0$ if $m \neq n$ and $\delta_{n,n} = 1$.

This matrix has a very strong structure, which can be expressed in terms of the well known rectangular Toeplitz matrix

$$\mathbf{T}_M = \begin{pmatrix} -1 & 2 & -1 & & 0 \\ & \ddots & \ddots & \ddots & \\ 0 & & -1 & 2 & -1 \end{pmatrix} \quad (10)$$

of M rows and $M + 2$ columns, related to the second-difference operator.

The following results are referred to the case where $N \geq K$, since this condition is what is usually satisfied in practice. It is also the most interesting from the mathematical point of view. When $N < K$ a specific case study can be carried out and this is discussed in appendix A.

Definition 2.1. For a fixed M , the $M \times M$ permutation matrix $\mathbf{\Pi}_M$ groups together the canonical basis vectors $\{e_j\}_{j=1}^M$ of \mathbb{R}^M according to the remainder of the subscript j divided by K . More precisely, let

$$J_r = \{j \in \{1, \dots, M\} : j \equiv r \pmod{K}\} \quad (11)$$

for $r = 1, \dots, K$; then

$$\mathbf{\Pi}_M = ((e_j)_{j \in J_1} | (e_j)_{j \in J_2} | \dots | (e_j)_{j \in J_K}). \quad (12)$$

Now assume that q and K_1 are the quotient and the remainder of the Euclidean division of N by K , respectively; that is, $N = qK + K_1$. It turns out that $\mathbf{\Pi}_N$ can be partitioned into K_1 blocks of $q + 1$ columns, followed by $K - K_1$ blocks of q columns. The same holds for $\mathbf{\Pi}_{N+2K}$, but in this case the number of columns is $q + 3$ for each block of the first group, $q + 2$ for the last blocks.

It is now immediate to prove the following.

Theorem 2.1. The matrix $\bar{\mathbf{T}} = \mathbf{\Pi}_N^T \mathbf{A} \mathbf{\Pi}_{N+2K}$ has a block diagonal pattern:

$$\begin{aligned} \bar{\mathbf{T}} &= \text{diag}(\underbrace{\mathbf{T}_{q+1}, \dots, \mathbf{T}_{q+1}}_{K_1 \text{ blocks}}; \underbrace{\mathbf{T}_q, \dots, \mathbf{T}_q}_{K-K_1 \text{ blocks}}) \\ &= \begin{pmatrix} \mathbf{I}_{K_1} \otimes \mathbf{T}_{q+1} & 0 \\ 0 & \mathbf{I}_{K-K_1} \otimes \mathbf{T}_q \end{pmatrix} \end{aligned} \quad (13)$$

where \mathbf{I}_M is the $M \times M$ identity matrix and \otimes is the Kronecker product.

Now it is easily observed that \mathbf{A} is a full-rank matrix. As a consequence, the null space of \mathbf{A} has dimension $2K$.

In appendix B we derive a set of $2K$ linearly independent vectors (in general, not orthogonal) which span the null space of \mathbf{A} . They are given by

$$(\mathbf{p}_k)_n = \exp\left(i2\pi \frac{k}{K} n\right) \quad (\mathbf{q}_k)_n = n(\mathbf{p}_k)_n \quad (n = 1, 2, \dots, N + 2K) \quad (14)$$

the index k taking the values $0, \pm 1, \dots, \pm(K - 1)/2$ if K is *odd* and the values $0, \pm 1, \dots, \pm(K - 2)/2, K/2$ if K is *even*. In this case we have only one \mathbf{p} -vector associated with $k = K/2$, which is given by $(\mathbf{p}_{K/2})_n = (-1)^n$. We remark that, if we assume $\Delta = K\delta$, then $2\pi k/K = (2\pi k/\Delta)\delta = \omega_{y,k}\delta$ and therefore the frequencies of the vectors \mathbf{p} , \mathbf{q} are related to the missed frequencies of equation (6).

In appendix B an orthogonal basis of the null space is also given.

The ill-conditioning of the matrix \mathbf{A} can be determined by computing its singular value decomposition (SVD) which, as is well known, is given by the following factorization

$$\mathbf{A} = \mathbf{U}\mathbf{\Sigma}\mathbf{V}^T \quad (15)$$

where $\mathbf{\Sigma}$ is the diagonal matrix $N \times N$ formed with the singular values σ_k of \mathbf{A} while \mathbf{U} and \mathbf{V} are isometric matrices, respectively $N \times N$ and $(N + 2K) \times N$, formed with the singular vectors \mathbf{u}_k , \mathbf{v}_k of \mathbf{A} .

The knowledge of the structure of \mathbf{A} allows us to obtain complete information about the singular values.

Theorem 2.2. Let $\tau_1^{(q)} \geq \dots \geq \tau_q^{(q)} > 0$ be the singular values of the Toeplitz matrix \mathbf{T}_q , and in the same way define $\{\tau_k^{(q+1)}\}_{k=1}^{q+1}$ as the singular values of \mathbf{T}_{q+1} .

Then the singular values $\sigma_1 \geq \dots \geq \sigma_N$ of \mathbf{A} are

$$\begin{cases} \tau_1^{(q+1)}, \dots, \tau_{q+1}^{(q+1)} & \text{counted with multiplicity } K_1 \\ \tau_1^{(q)}, \dots, \tau_q^{(q)} & \text{counted with multiplicity } K - K_1. \end{cases} \quad (16)$$

Moreover, the ratio $\alpha = \sigma_1/\sigma_N$ is asymptotical to $4q^2/\pi^2$.

Proof. We determine the σ_k 's as the square roots of the eigenvalues of \mathbf{AA}^T . In the light of theorem 2.1, the following holds:

$$\mathbf{AA}^T = (\mathbf{\Pi}_N \bar{\mathbf{\Pi}} \mathbf{\Pi}_{N+2K}^T) (\mathbf{\Pi}_{N+2K} \bar{\mathbf{\Pi}}^T \mathbf{\Pi}_N^T) = \mathbf{\Pi}_N \bar{\mathbf{D}} \mathbf{\Pi}_N^T \quad (17)$$

where

$$\bar{\mathbf{D}} = \bar{\mathbf{\Pi}} \bar{\mathbf{\Pi}}^T = \begin{pmatrix} \mathbf{I}_{K_1} \otimes (\mathbf{T}_{q+1} \mathbf{T}_{q+1}^T) & 0 \\ 0 & \mathbf{I}_{K-K_1} \otimes (\mathbf{T}_q \mathbf{T}_q^T) \end{pmatrix}. \quad (18)$$

Hence, \mathbf{AA}^T is similar up to permutation to the block diagonal matrix $\bar{\mathbf{D}}$, whose spectrum is given by that of $\mathbf{T}_{q+1} \mathbf{T}_{q+1}^T$, repeated K_1 times, joint with that of $\mathbf{T}_q \mathbf{T}_q^T$, repeated $K - K_1$ times; this justifies relations (16).

In order to prove the last part of the statement, observe from (16) that $\sigma_1 = \max(\tau_1^{(q)}, \tau_1^{(q+1)})$ and $\sigma_N = \min(\tau_q^{(q)}, \tau_{q+1}^{(q+1)})$.

A direct calculation shows that, for $M = q$ or $q + 1$,

$$\mathbf{T}_M \mathbf{T}_M^T = \begin{pmatrix} 6 & -4 & 1 & & 0 \\ -4 & \ddots & \ddots & \ddots & \\ 1 & \ddots & \ddots & \ddots & 1 \\ & \ddots & \ddots & \ddots & -4 \\ 0 & & 1 & -4 & 6 \end{pmatrix} =: \mathbf{D}_M. \quad (19)$$

Therefore, the singular values of \mathbf{T}_M are the square roots of the eigenvalues of \mathbf{D}_M .

By the Cauchy interlace theorem [3] we have

$$\lambda_{\min}(\mathbf{D}_{q+1}) \leq \lambda_{\min}(\mathbf{D}_q) \leq \lambda_{\max}(\mathbf{D}_q) \leq \lambda_{\max}(\mathbf{D}_{q+1}) \quad (20)$$

so that $\sigma_1 = \tau_1^{(q+1)} = \sqrt{\lambda_{\max}(\mathbf{D}_{q+1})}$, $\sigma_N = \tau_{q+1}^{(q+1)} = \sqrt{\lambda_{\min}(\mathbf{D}_{q+1})}$.

In the literature one can find tight asymptotical estimates for the eigenvalues of symmetric Toeplitz matrices like \mathbf{D}_{q+1} , see for example [4]. It follows that

$$\lambda_{\max}(\mathbf{D}_{q+1}) \sim 16 \quad \lambda_{\min}(\mathbf{D}_{q+1}) \sim \frac{\pi^4}{q^4} \quad (21)$$

hence $\alpha = \sigma_1/\sigma_N \sim 4q^2/\pi^2$ and the thesis is proved. \square

For a given value of N , the singular value spectrum of \mathbf{A} and its ill-conditioning depend on the value of the chopping amplitude K . In the light of theorem 2.2 the condition number of \mathbf{A} , defined by $\alpha = \sigma_1/\sigma_N$, only depends on the *quotient* between N and K , and therefore is a decreasing function of K .

In order to quantify this statement we give numerical results in the case $N = 128$, which is a typical value of the dimension of a chopped and nodded image obtained with present day thermal-infrared detectors [5, 6]. The behaviour of α as a function of K is shown in figure 1

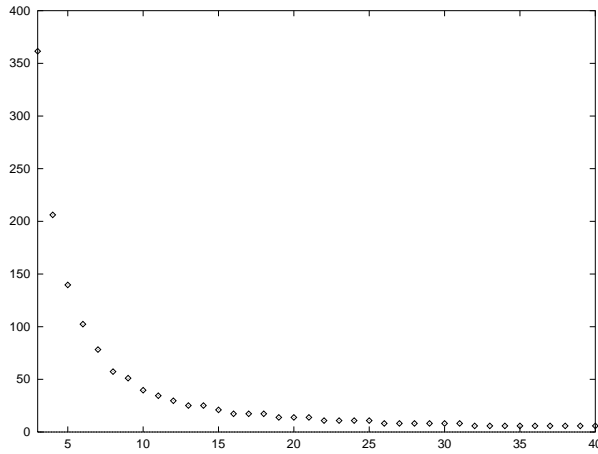


Figure 1. Behaviour of the condition number α as a function of the chopping amplitude K in the case $N = 128$.

where we consider K varying from 3 up to 40. Indeed, values of K smaller than 3 can hardly be obtained, taking into account the usual sampling of infrared images. On the other hand, values of K greater than 40 ($q = 3$) are not frequently used in practice.

In the region considered α decreases from the value $\alpha = 362$ for $K = 3$ to the value $\alpha = 5.8$ for $K = 40$.

In conclusion, we point out an important practical consequence of theorem 2.2. For a given image corresponding to a given chopping amplitude, the values of N and K depend on the choice of the sampling distance δ . The quotient between N and K , however, does not depend on δ and is essentially the quotient between the size X of the image and the chopping amplitude Δ , both measured in seconds of arc. Since the condition number $\alpha = \sigma_1/\sigma_N$ is the quantity which controls noise propagation in the inversion algorithm, it is important to reduce this quantity by reducing the quotient q . This can be obtained by increasing the chopping amplitude Δ for a given size X of the image or by considering a convenient sub-image for a given chopping amplitude.

If we decide, for instance, that only values smaller than 10 are acceptable for the condition number, then from figure 1 we deduce that q must be smaller than 6, i.e. X and Δ must be chosen in such a way that $\Delta > X/6$.

3. The generalized solution

The equation $\mathbf{A}\mathbf{f} = \mathbf{g}$ to be solved has infinitely many solutions, since \mathbf{A} has a $2K$ -dimensional null space as discussed in the previous section. Hence we can look for the *generalized solution* \mathbf{f}^\dagger having minimal Euclidean norm, given by the formula

$$\mathbf{f}^\dagger = \mathbf{A}^\dagger \mathbf{g} \quad \mathbf{A}^\dagger = \mathbf{A}^T (\mathbf{A}\mathbf{A}^T)^{-1} \quad (22)$$

\mathbf{A}^\dagger being the $(N + 2K) \times N$ generalized inverse of \mathbf{A} .

The characterization of \mathbf{A} shown in theorem 2.1 readily yields an explicit expression of \mathbf{A}^\dagger in terms of the generalized inverses of the matrices \mathbf{T}_q and \mathbf{T}_{q+1} . It turns out that

$$\mathbf{A}^\dagger = \mathbf{\Pi}_{N+2K} \bar{\mathbf{T}}^\dagger \mathbf{\Pi}_N^T \quad \bar{\mathbf{T}}^\dagger = \begin{pmatrix} \mathbf{I}_{K_1} \otimes \mathbf{T}_{q+1}^\dagger & 0 \\ 0 & \mathbf{I}_{K-K_1} \otimes \mathbf{T}_q^\dagger \end{pmatrix}. \quad (23)$$

This implies that \mathbf{A}^\dagger mimics the pattern of \mathbf{A} , but in this case \mathbf{A}^\dagger exhibits $2q + 3$ (not just 3) significant diagonals interlaced by groups of $K - 1$ null diagonals and flanked by two groups of $K_1 - 1$ null diagonals.

Remark 3.1. It is worth pointing out that, in view of (23), every significant diagonal is *piecewise constant*: more precisely, the first element is repeated K_1 times, then it changes to a second value which stays constant for $K - K_1$ times. Next a third value appears which is repeated again K_1 times and so on. Thus, we detect *jumps* on the diagonals of \mathbf{A}^\dagger in correspondence to the rows $K_1, K, K + K_1, 2K, \dots, K_1 + (q + 1)K, (q + 2)K$ ($2q + 4$ jumps). As we will see, this structure generates artifacts in the restored images.

Another implication of the structure of \mathbf{A}^\dagger is the following expression for \mathbf{f}^\dagger : if we partition $\Pi_N^T \mathbf{g}$ in K subvectors \mathbf{g}_j , for which the first K_1 contain $q + 1$ elements and the others q elements, then

$$\mathbf{f}^\dagger = \Pi_{N+2K} \begin{pmatrix} \mathbf{T}_{q+1}^\dagger \mathbf{g}_1 \\ \vdots \\ \mathbf{T}_{q+1}^\dagger \mathbf{g}_{K_1} \\ \mathbf{T}_q^\dagger \mathbf{g}_{K_1+1} \\ \vdots \\ \mathbf{T}_q^\dagger \mathbf{g}_K \end{pmatrix}. \quad (24)$$

Thus, computing the generalized solution is equivalent to solving K independent subproblems, each of size q or $q + 1$.

As is well known, the generalized inverse \mathbf{A}^\dagger can also be computed by computing the SVD of \mathbf{A} . This computation is simplified by the representation of \mathbf{A} provided by theorem 2.1, because it is reduced to the computation of the singular systems of the matrices \mathbf{T}_q and \mathbf{T}_{q+1} . Then the generalized inverse \mathbf{A}^\dagger is obtained by means of the SVD of \mathbf{A} as follows:

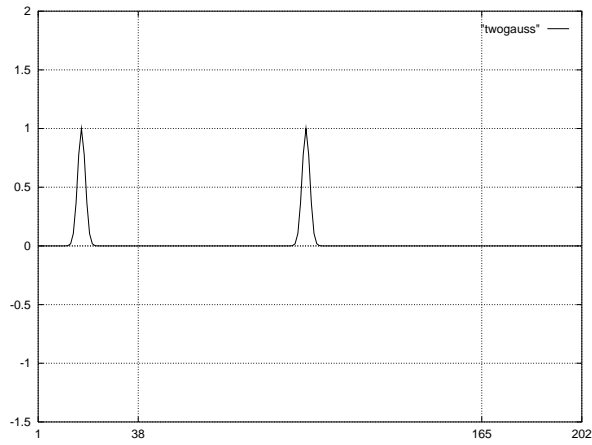
$$\mathbf{A}^\dagger = \mathbf{V} \Sigma^{-1} \mathbf{U}^T \quad (25)$$

and finally \mathbf{f}^\dagger is given by the first of equations (22).

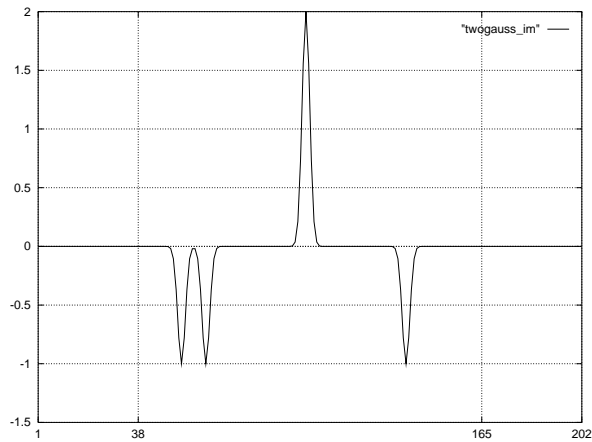
The generalized solution is orthogonal to the null space of the matrix \mathbf{A} , i.e. the subspace of the objects whose chopped and noded images are zero. In particular, \mathbf{f}^\dagger is orthogonal to \mathbf{p}_0 , equation (14), and therefore the sum of the components of \mathbf{f}^\dagger is zero. This can be a rather serious limitation and, consequently, the restoration provided by \mathbf{f}^\dagger may be unsatisfactory from the practical point of view.

In order to verify this statement we have performed a few numerical simulations both in the one- (1D) and two-dimensional (2D) cases. In the case of 2D images, (22) and (25) must be used for each column of the image (if the chopping is in the y -direction). In these simulations we do not add noise to the chopped and noded images because the main interest is to investigate the effect of the orthogonality of the generalized solution to the null space of \mathbf{A} .

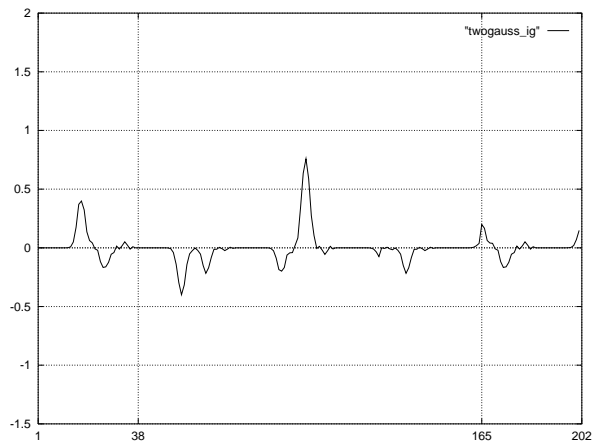
In figure 2 we give two numerical examples of 1D restorations. In the left column the object consists of two narrow Gaussian functions (simulating two bright stars over a black background), one inside and one outside the observation region. Since $N = 128$ and $K = 37$ ($q = 3$), the object consists of 202 points and the observation region corresponds to the points from $n = 38$ to $n = 165$. The chopped and noded image contains not only the two negative ghosts of the star in the observation region but also a negative ghost of the external one. The restoration provided by the generalized inverse underestimates the



(a.1)

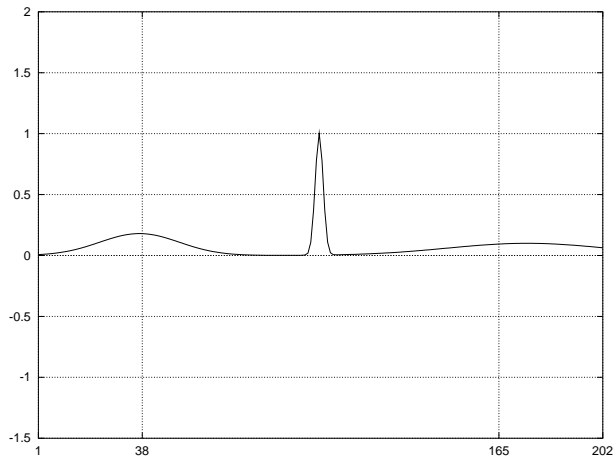


(b.1)

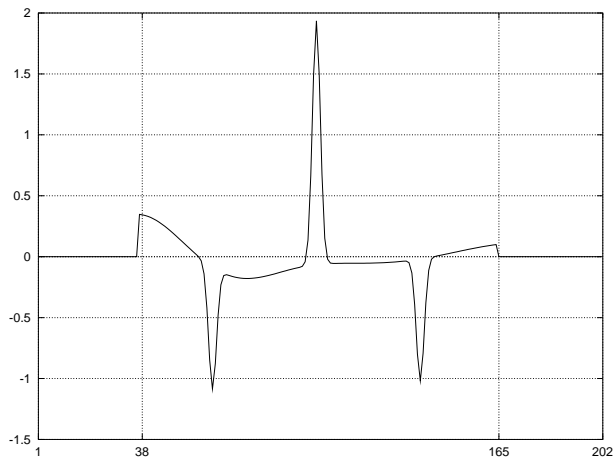


(c.1)

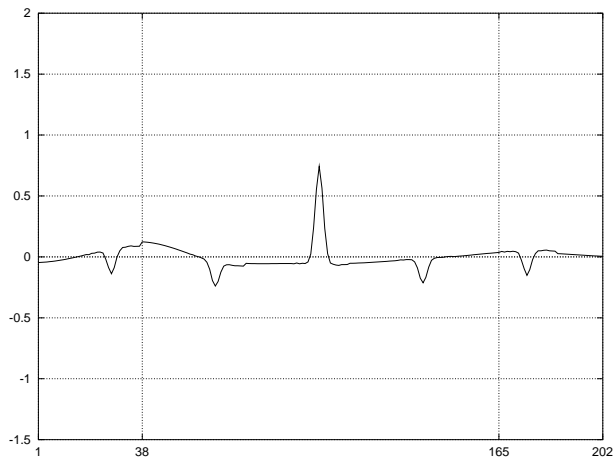
Figure 2. (a.1) The object; (b.1) the chopped and noded image; (c.1) the restoration provided by the generalized inverse. (a.2) The object; (b.2) the chopped and noded image; (c.2) the restoration provided by the generalized inverse. The vertical lines indicate the observation region.



(a.2)

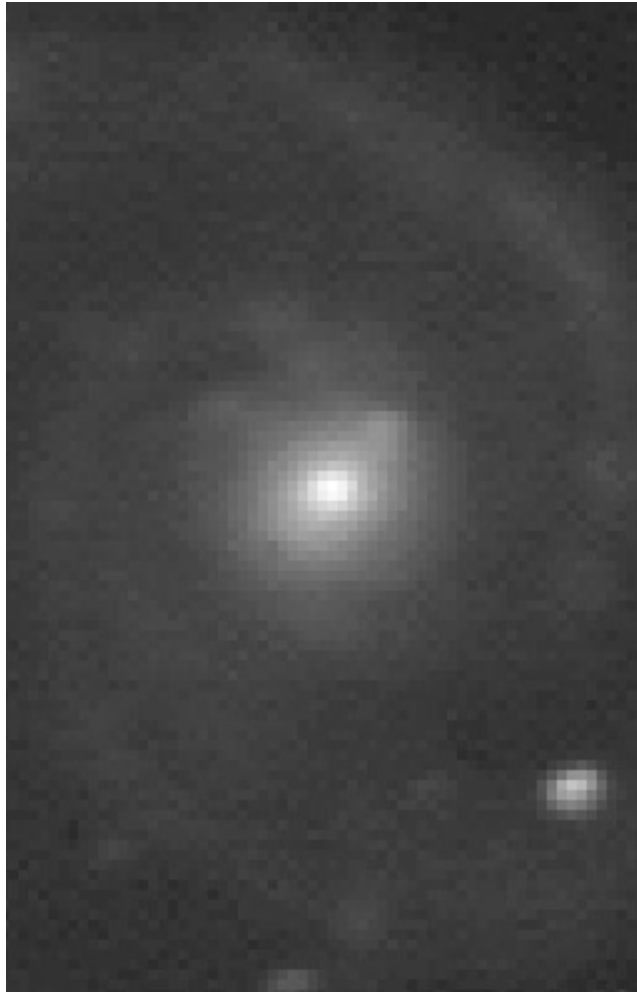


(b.2)



(c.2)

Figure 2. (Continued)



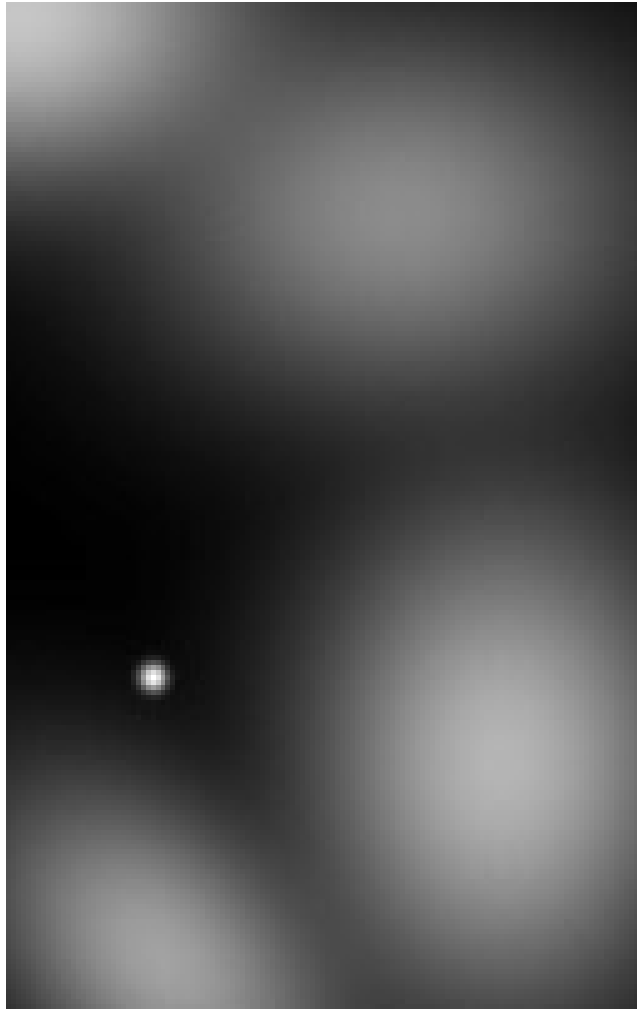
(a)

Figure 3. (a) 202×128 image of the nucleus of the M51 galaxy; (b) 202×128 image simulating a bright star surrounded by weaker clouds. Both images are represented using a square-root grey scale.

two Gaussian peaks and produces a rather complicated structure consisting of negative and positive ghosts. The non-conservation of the flux is a critical problem from the point of view of astronomical photometry and, considering also the significant artifacts, it turns out that this result is completely unsatisfactory.

In the right column the object consists of three Gaussian functions, one narrow, simulating a bright star inside the observation region and two broad, simulating a slowly varying background. Even if the restoration looks better than the previous one, the result is not yet satisfactory also because the height of the peak is underestimated.

In the case of 2D images we have considered two synthetic objects. The first is obtained by extracting from a 256×256 image of the M51 galaxy, a 202×128 image containing the nucleus of the galaxy. The second is a 202×128 image, generated by means of five 2D Gaussian functions, simulating a bright star surrounded by weaker clouds (approximately a factor of

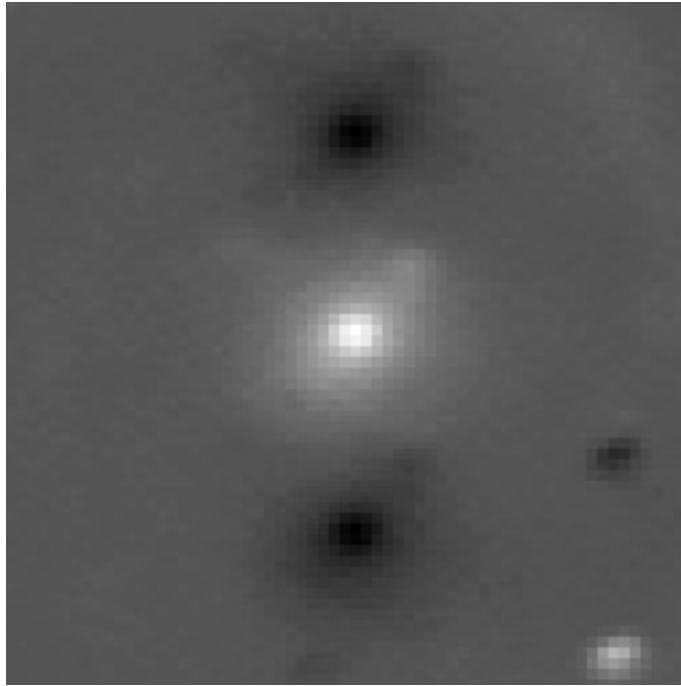


(b)

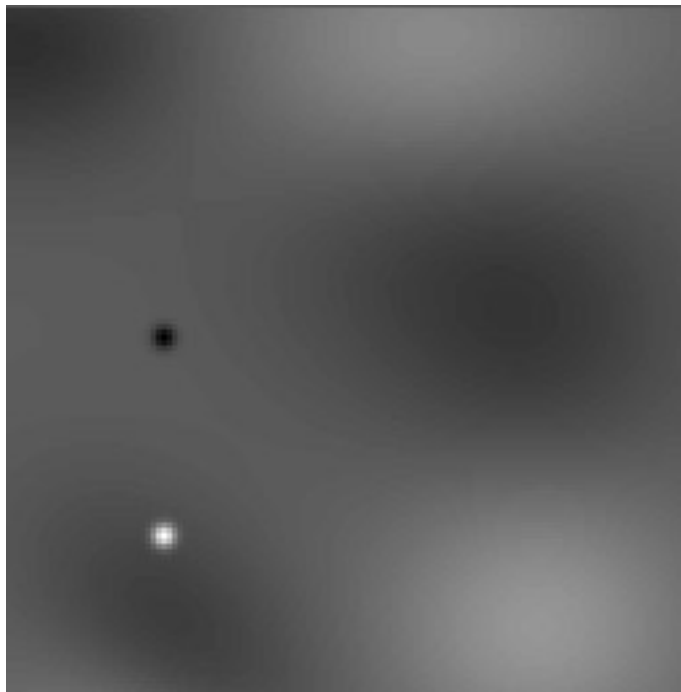
Figure 3. (Continued)

two between the maximum value of the star and the maximum values of the clouds). The two images are given in figure 3. The corresponding chopped and noded images, 128×128 , obtained with a chopping amplitude $K = 37$, are given in figure 4. In both cases the negative ghosts of the bright objects are evident. Finally, the restorations provided by the generalized inverse, again 202×128 , are given in figure 5.

In both examples we find that the generalized solution still contains multiple negative versions (ghosts) of the brightest objects in the original image. These ghosts are spaced by K , the chopping amplitude. Moreover, the restoration shown in figure 5(b) exhibits jumps at the rows $K_1, K, K_1 + K, \dots$, due to the structure of the diagonals of the matrix \mathbf{A}^\dagger , as described in remark 3.1. Indeed, this structure determines several discontinuities in the application of the generalized inverse to the smooth image g . In this particular example we also observe that the main jumps are accompanied by a finer structure of smaller jumps. In any case all these results indicate that the restoration provided by the generalized inverse is completely unsatisfactory.

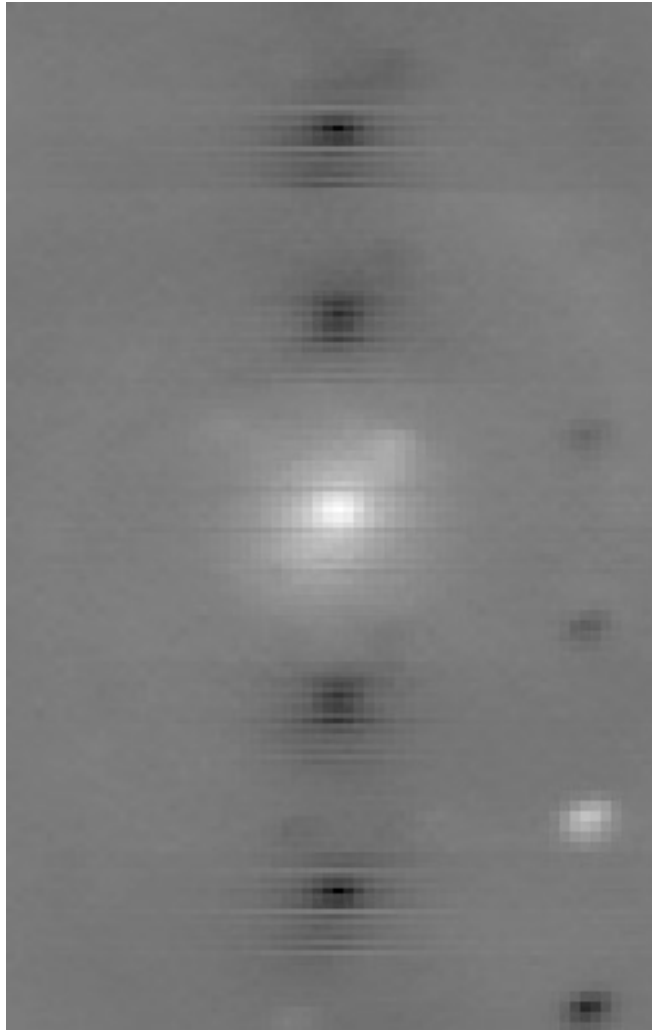


(a)



(b)

Figure 4. (a) Chopped and noded image, 128×128 , of the nucleus of the M51 galaxy, given in figure 3(a) ($K = 37$); (b) chopped and noded image, 128×128 , of the object of figure 3(b) ($K = 37$). Both images are represented using a linear grey scale.

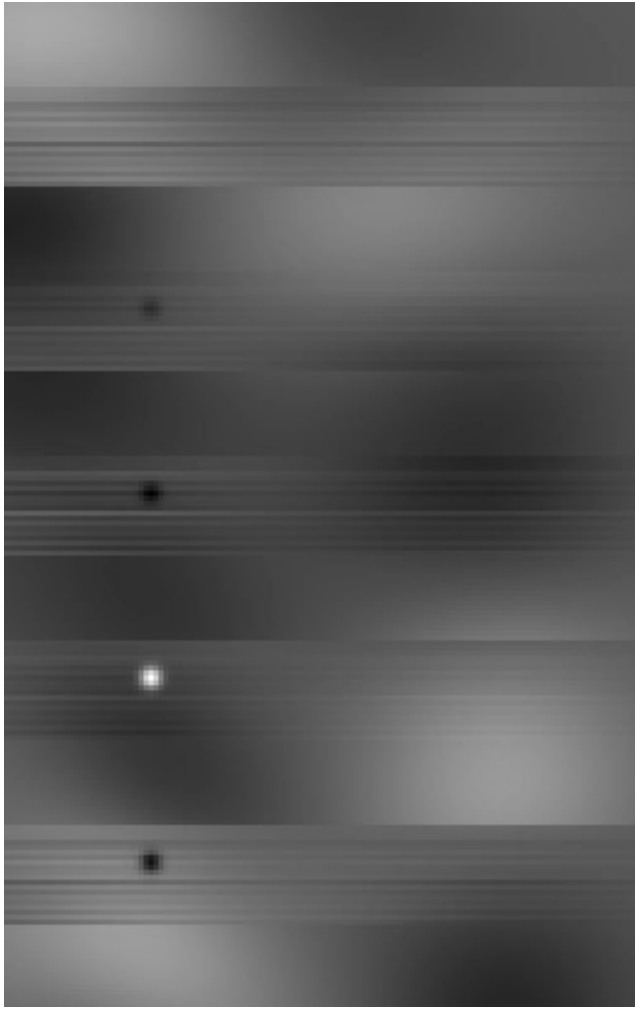


(a)

Figure 5. (a) Restoration of the nucleus of the M51 galaxy obtained by means of the generalized inverse from the chopped and noddied image of figure 4(a); (b) restoration of the synthetic object of figure 3(b), obtained by means of the generalized inverse from the chopped and noddied image of figure 4(b). Both images are represented using a square-root grey scale.

4. The positive solution of minimal norm

As shown in the previous section, the generalized solution takes negative values which can be very large. This property is unavoidable since the sum of the components of \mathbf{f}^\dagger must be zero. On the other hand, the brightness distribution which has generated the chopped and noddied image is certainly non-negative and to this purpose it is important to point out that the equation $\mathbf{A}\mathbf{f} = \mathbf{g}$ has non-negative solutions. Indeed, by taking any solution of this equation and adding to it a sufficiently large and positive constant vector, which is proportional to \mathbf{p}_0 (see equation (14)), one gets another solution of the same equation which is now non-negative. Such a solution, however, may be deprived of any physical interest.



(b)

Figure 5. (Continued)

It is easy to recognize that the set of non-negative solutions is closed and convex so that it has a unique element of minimal Euclidean norm, which will be denoted by \mathbf{f}_+^\dagger . We intend to investigate if it can provide a satisfactory solution of the restoration problem.

The problem of computing \mathbf{f}_+^\dagger can be ill-conditioned in the sense that a small error on the data can produce a large error on \mathbf{f}_+^\dagger . Therefore, we not only need a method for computing \mathbf{f}_+^\dagger but also a method which can eventually produce a regularized approximation of \mathbf{f}_+^\dagger .

For this purpose, let us remark that the set of non-negative solutions of the basic equation $\mathbf{A}\mathbf{f} = \mathbf{g}$ coincides with the set of the non-negative least-squares solutions, i.e. the solutions of the following constrained minimization problem

$$\|\mathbf{A}\mathbf{f} - \mathbf{g}\|_2 = \text{minimum} \quad \mathbf{f} \geq 0 \quad (26)$$

where $\|\cdot\|_2$ denotes the Euclidean norm. Then, an iterative method for approximating the solutions of this problem is provided by the so-called projected Landweber method [7] which

is given by

$$\mathbf{f}^{(k+1)} = P_+[\mathbf{f}^{(k)} + \tau(\mathbf{A}^T \mathbf{g} - \mathbf{A}^T \mathbf{A} \mathbf{f}^{(k)})] \quad (27)$$

where:

- P_+ is the convex projection onto the closed and convex set of the non-negative vectors

$$\begin{aligned} (P_+ \mathbf{f})_n &= f_n & \text{if } f_n > 0 \\ &= 0 & \text{if } f_n \leq 0 \end{aligned} \quad (28)$$

- τ is the relaxation parameter, which can take any value satisfying the inequalities

$$0 < \tau < \frac{2}{\sigma_1^2} \quad (29)$$

where σ_1 is the largest singular value of the matrix \mathbf{A} .

It is known that, for any initial guess $\mathbf{f}^{(0)}$, the sequence of the iterates $\mathbf{f}^{(k)}$ converges to a solution of the least-squares problem (26) [8]. The limit depends on the initial guess $\mathbf{f}^{(0)}$ since the solution of the problem is not unique. As far as we know, it has not yet been established what initial guess is suitable for obtaining a sequence converging to \mathbf{f}_+^\dagger . Presumably, it is the vector which is identically zero and this is the choice we have assumed to be the correct one, i.e. we have initialized the iterative procedure (27) with

$$\mathbf{f}^{(0)} = \mathbf{0}. \quad (30)$$

As already pointed out, \mathbf{f}_+^\dagger may not be the interesting solution in the case of noisy data because the effect of noise on it may be unacceptable. In such a case numerical experiments indicate that the projected Landweber method has the *semiconvergence property* [7]: the iterates first approach the solution of the problem corresponding to noise-free data and then go away. In other words equation (27) defines an iterative regularization method with the number of iterations acting as a regularization parameter. Then an important problem is how to choose this number of iterations. In the case of simulations using synthetic data an obvious criterion is to stop the iterations when the minimum of the restoration error is reached, while in the case of real data one can use the *discrepancy principle* [9]: if an estimate of the Euclidean norm of the noise is known, then the iterations are stopped when the residual, which is a decreasing function of the number of iterations, becomes smaller than this estimate. All these points will be reconsidered in the following section.

5. Implementation and validation of the method

Since the convergence of the projected Landweber method is, in general, rather slow [7], an efficient implementation is very important. To this purpose, two points must be considered.

The first is the computation of the matrix-vector product $\mathbf{A}^T \mathbf{A} \mathbf{f}$. In this case one can take advantage of the fact that $\mathbf{A}^T \mathbf{A}$ has at most five significant diagonals. In appendix C we give explicit expressions of $\mathbf{A}^T \mathbf{A} \mathbf{f}$ which, when used, require a number of operations proportional to N . In the practical case $N > K$, the two possibilities $N > 2K$ and $N < 2K$ must be considered and implemented separately.

The second point is the choice of the relaxation parameter because the convergence rate depends on this parameter. Numerical practice indicates that the number of iterations, required for obtaining a certain accuracy of the solution, first decreases with increasing τ and then increases when τ approaches the upper limit, because for $\tau = 2/\sigma_1^2$ the method does not converge [7]. Therefore, a value of τ not too close to, but also not too far from, the upper limit is preferable. We choose $\tau = 1.8\sigma_1^{-2}$ and since $\sigma_1^2 \leq 16$, we take for simplicity $\tau = 0.1$.

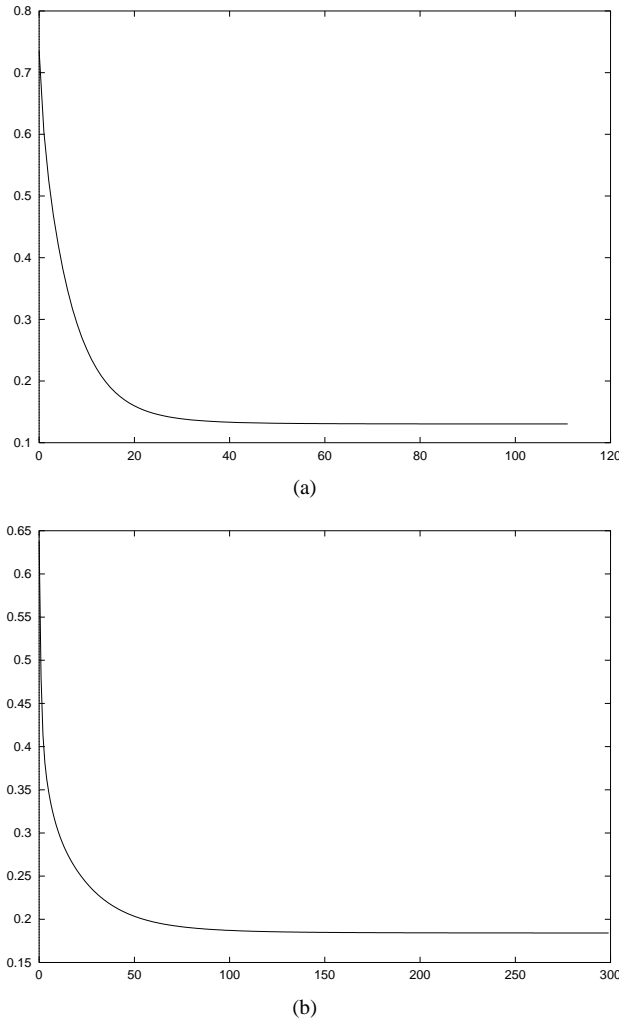


Figure 6. Behaviour of $\varrho^{(k)}$, equation (32), as a function of the number of iterations k , for the two examples of figure 2.

In the case of 2D images the algorithm is applied to each column of the image.

In our code, we have options for computing the following quantities at each iteration step:

(a) the relative discrepancy defined by

$$\varepsilon^{(k)} = \frac{\|\mathbf{A}\mathbf{f}^{(k)} - \mathbf{g}\|_2}{\|\mathbf{g}\|_2} \quad (31)$$

where $\|\cdot\|_2$ denotes the Euclidean norm of the vector (in 1D restorations) or of the image (in 2D restorations), i.e. $\varepsilon^{(k)}$ is the relative root-mean-square (RMS) error we commit if we compute the chopped and noded image by means of $\mathbf{f}^{(k)}$ ($\varepsilon^{(k)}$ can also be called the relative residual);

(b) in the case of simulations (synthetic data), the relative restoration error defined by

$$\varrho^{(k)} = \frac{\|\tilde{\mathbf{f}}^{(k)} - \mathbf{f}\|_2}{\|\mathbf{f}\|_2} \quad (32)$$

where \mathbf{f} is the original object and $\tilde{\mathbf{f}}^{(k)}$ is a rescaled version of $\mathbf{f}^{(k)}$, having the same offset

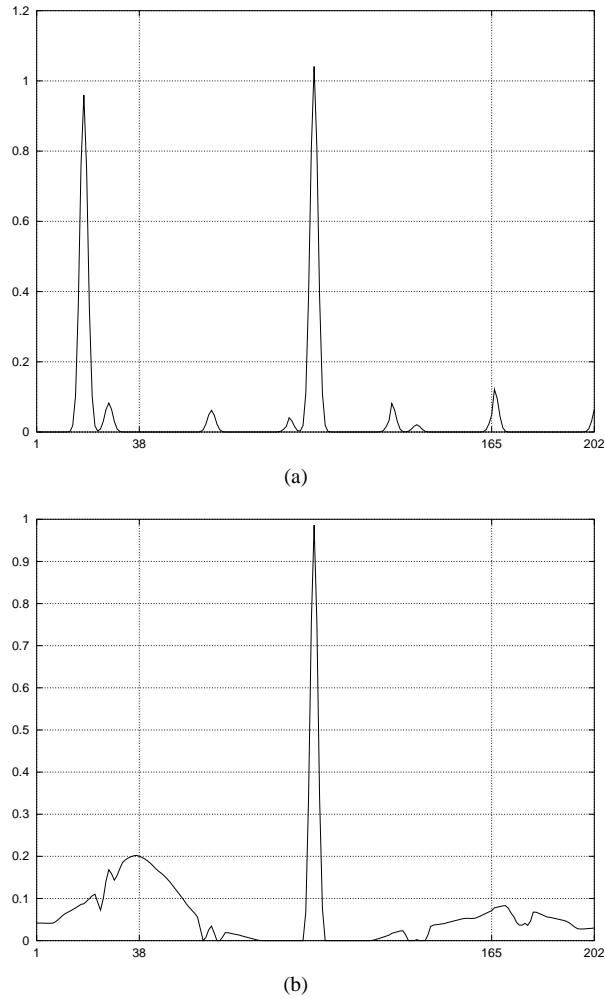


Figure 7. Restorations provided by the positive solution of minimal norm for the two examples of figure 2.

as \mathbf{f} , i.e.

$$\tilde{\mathbf{f}}^{(k)} = \mathbf{f}^{(k)} + \text{offset}[\mathbf{f} - \mathbf{f}^{(k)}] \quad (33)$$

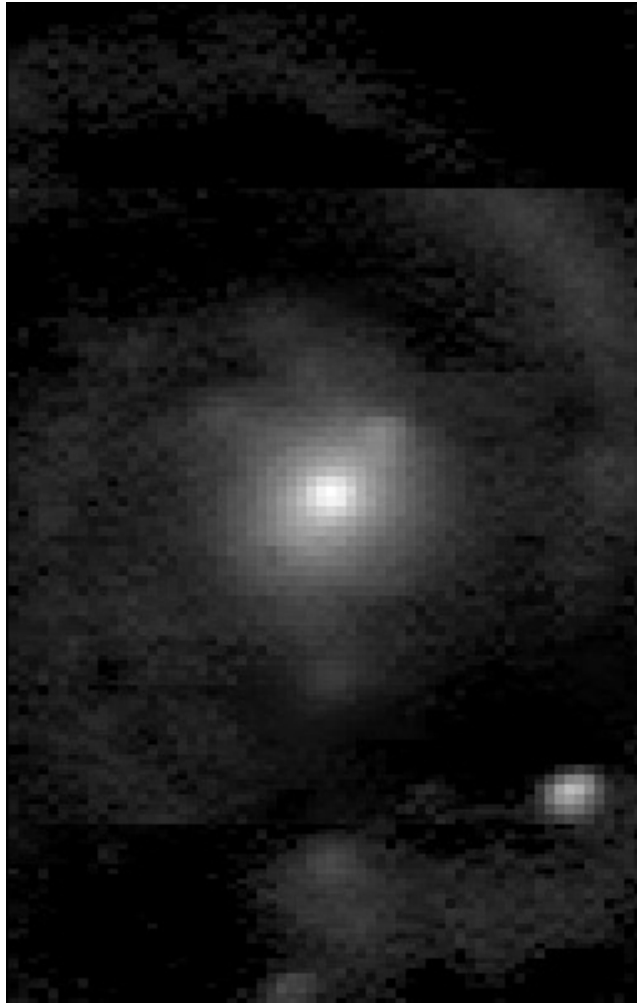
where

$$\text{offset}[\mathbf{f}] = \frac{1}{N^2} \sum_{i,j=1}^N f_{ij}. \quad (34)$$

For 1D restorations, the factor $1/N^2$ in equation (34) must be replaced by $1/N$. The restoration error (32) can also be computed by restricting both \mathbf{f} and $\tilde{\mathbf{f}}^{(k)}$ to the observation region. In such a case it will be denoted by $\varrho_{OR}^{(k)}$.

Our algorithm, written in C, is fast and an image 128×128 can be processed in a few seconds on a Pentium 200.

In the case of synthetic data the iterations are stopped when $\varrho^{(k)}$ reaches its minimum value; on the other hand, in the case of real data, the iterations are stopped at that value k_0



(a)

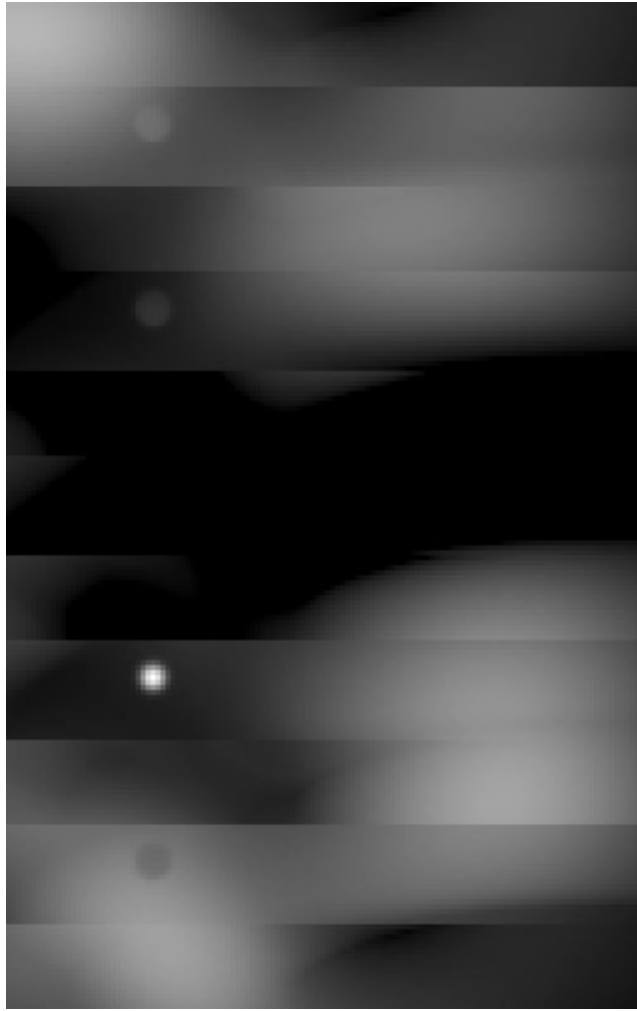
Figure 8. (a) Restoration of the object of figure 3(a), obtained by means of the projected Landweber method, using the chopped and noded image of figure 4(a); (b) restoration of the object of figure 3(b), obtained by means of the projected Landweber method, using the chopped and noded image of figure 4(b).

such that

$$\varepsilon^{(k_0)} \geq \varepsilon \quad \varepsilon^{(k_0+1)} < \varepsilon \quad (35)$$

where ε is an estimate of the relative RMS error on the data. We point out that the value of k_0 is uniquely defined because, as follows from general results on the projected Landweber method [8], $\varepsilon^{(k)}$ is a decreasing function of k which tends to zero when $k \rightarrow \infty$.

The method described has been applied to the numerical examples of section 3. We have first considered the 1D examples and we have checked the convergence of the method by computing the restoration error $\varrho^{(k)}$, equation (32). Since in this first application, we do not add noise to the chopped and noded images, the limit of $\varrho^{(k)}$ for $k \rightarrow \infty$ is the approximation error intrinsic to the positive solution of minimal norm (with offset correction).



(b)

Figure 8. (Continued)

In figure 6 we give the behaviour of $\varrho^{(k)}$ for the two examples of figure 2.

In the case of the first example, corresponding to the two bright stars (left curve), the limit is reached after 40 iterations and the restoration error is 13.3% while the error on the observation region is 11.8%. In the case of the second example the limit is reached after 100 iterations and the restoration error is 18.7%. When we consider the observation region, the restoration error is much smaller, 12.7%. The corresponding restorations are given in figure 7.

As concerns the first example we observe that the heights of the two Gaussian peaks are now correctly estimated. The restoration error is mainly due to the appearance of small positive multiple images of the two main peaks, approximately at the positions of the negative ghosts in the generalized solution (figure 2). Also in the second example the height of the main Gaussian peak is correctly reproduced while the slowly varying background is perturbed by the multiple images of the main peak which now tend to lower its value. These effects will be even more evident in the 2D examples.

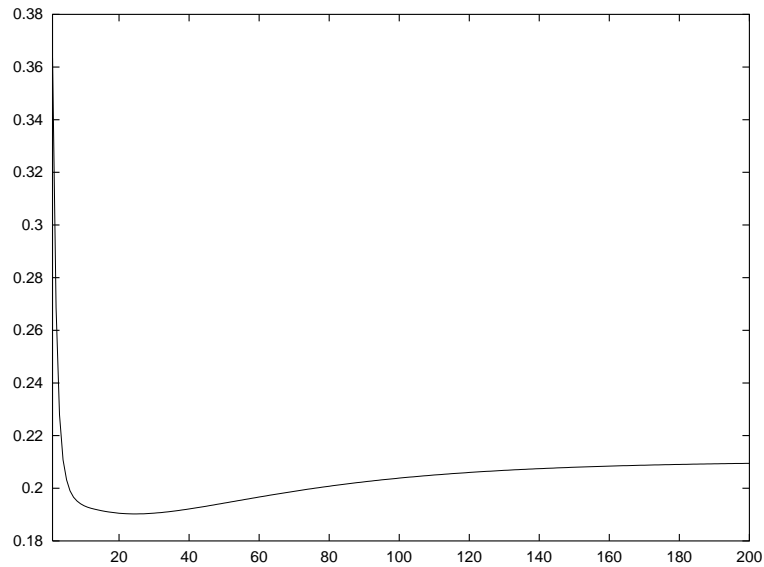


Figure 9. Behaviour of $\rho^{(k)}$, equation (32), for the second example of figure 2, in the case of a noisy image ($\varepsilon = 15.6\%$).

The restoration of the 2D examples of figure 3 is given in figure 8. The limiting errors on the observation region are respectively 4.5% for the M51 galaxy and 22.5% for the synthetic image. They are reached respectively after 18 and 76 iterations.

As follows from the pictures of figure 8, the two examples have a rather different behaviour. In the restoration of M51, figure 8(a), no significant artifact appears in the observation region, in agreement with the small value of the restoration error. Only the jumps at the boundary of the observation region are evident. On the other hand, in the restoration of the second example, figure 8(b), two kinds of artifacts are apparent:

- multiple images of the star (the ghosts previously mentioned) which may appear as dark images over a bright background or as bright images over a dark background, at a distance from the original star which is a multiple of the chopping amplitude K ;
- discontinuities in the brightness distribution at the rows corresponding to the jumps in the diagonals of the generalized inverse.

The different behaviour of the two examples is probably due to the fact that, in the first case, the background is rather uniform and much smaller than the brightest objects while, in the second case, the background is strongly varying and comparable with the brightest object. A way to reduce the artifacts in such a case will be proposed in the next section.

Next we have investigated the effect of the noise. To all chopped and noded images we added white noise with a standard deviation equal to the 3% of the maximum value of the image. We give the result in the case of the second example of figure 2, since this is a good representative of the results obtained for the other examples.

For this particular example the standard deviation of the white noise is 0.06 and the corresponding value of ε , the relative RMS on the data, is 15.6%.

In figure 9 we plot the behaviour of the restoration error. We find the typical behaviour of an iterative regularization method: the restoration error has a minimum for a certain number of iterations (semiconvergence property).

Table 1. The number of iterations k_0 ($\varepsilon = 0.1\%$) and the relative restoration error ϱ_0 on the observation region for the example (a.1) of figure 2 and for various values of the chopping amplitude K .

	K			
	17	23	29	37
k_0	132	189	128	65
ϱ_0 (%)	5.1	9.1	8.4	11.8

Table 2. The number of iterations k_0 ($\varepsilon = 0.5\%$) and the relative restoration error ϱ_0 on the observation region for the example (a.2) of figure 2 and for various values of the chopping amplitude K .

	K			
	17	23	29	37
k_0	495	275	142	101
ϱ_0 (%)	10.4	9.9	11.4	12.7

Table 3. The number of iterations k_0 ($\varepsilon = 3\%$) and the relative restoration error ϱ_0 on the observation region for the example of figure 3(a) and for various values of the chopping amplitude K .

	K			
	17	23	29	37
k_0	41	29	22	18
ϱ_0 (%)	7.3	5.9	5.3	4.5

Table 4. The number of iterations k_0 ($\varepsilon = 3\%$) and the relative restoration error ϱ_0 on the observation region for the example of figure 3(b) and for various values of the chopping amplitude K .

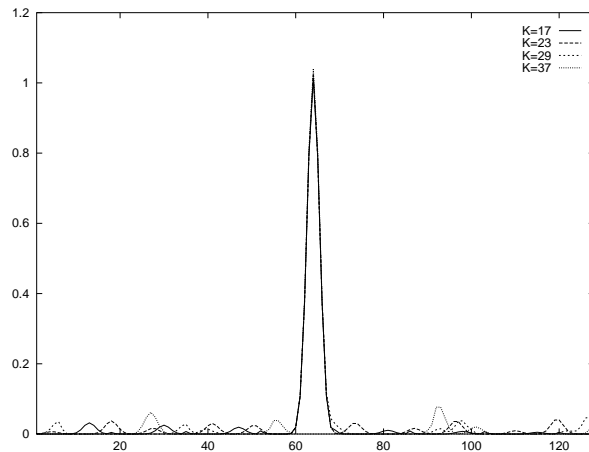
	K			
	17	23	29	37
k_0	538	234	129	76
ϱ_0 (%)	27.6	24.6	23.3	22.5

The minimum occurs after 34 iterations and the corresponding restoration error is 30.6%, while the restoration error on the region of interest is 19.1%. The relative discrepancy at the minimum, as defined in (31), is 3.37%. The values of the restoration errors are considerably larger than those obtained in the noise-free case (18.7% and 12.7%, respectively) and this fact indicates an important effect of the noise on the quality of the restoration, in spite of the rather small value of the condition number of the imaging matrix ($\alpha = 5.8$). However, we expect that the effect of the noise can be reduced by the method we propose in the next section.

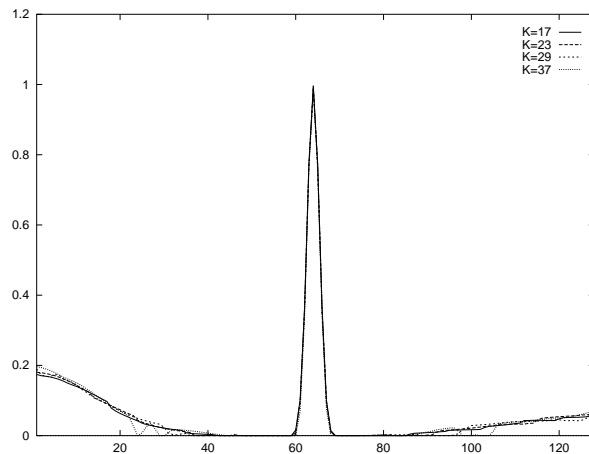
Finally, we have used the discrepancy principle for stopping the iterative procedure (see equation (35)). We obtain $k_0 = 3$ and the corresponding restoration errors are 42.6% and 26.8%, respectively.

6. A method for the reduction of the artifacts

Since the artifacts observed in the restorations provided by the projected Landweber method are related to K , a procedure for their reduction is rather obvious: measure various chopped and



(a)

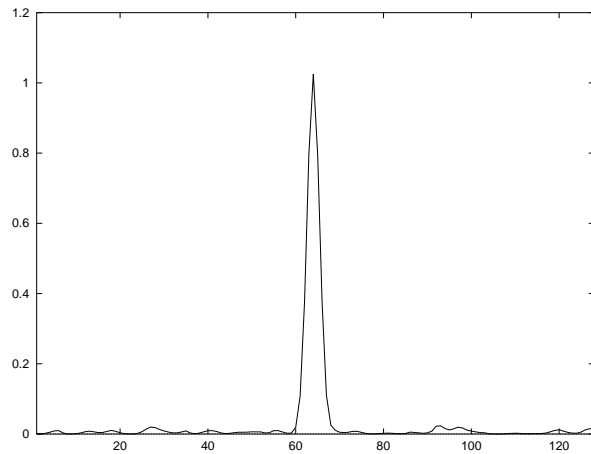


(b)

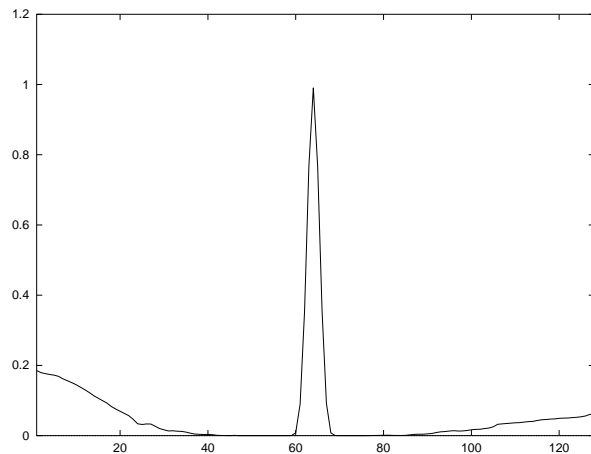
Figure 10. (a) Restorations of the first example of figure 2 on the observation region, corresponding to various values of K ; (b) restorations of the second example of figure 2 on the observation region, corresponding to various values of K ; (c) arithmetic mean of the restorations given in (a); (d) arithmetic mean of the restorations given in (b). Full curve, $K = 17$; dashed curve, $K = 23$; small-dashed curve, $K = 29$; dotted curve, $K = 37$.

noded images of the same brightness distribution obtained with different chopping amplitudes, restore all images by means of the projected Landweber method and take the average (arithmetic mean) of the restored images. This procedure is similar to that suggested by Beckers [1], at least as concerns the data acquisition, but it is completely different as concerns the data processing.

The procedure can be checked on the numerical examples used in the previous sections, by computing for each one of them various chopped and noded images corresponding to different values of K . The first problem is the choice of these values. We take $K = 17, 23, 29, 37$, so that the corresponding values of q and K_1 are $q = 7, 5, 4, 3$ and $K_1 = 9, 13, 12, 17$, while the numbers of discontinuity lines in the observation region are $2q = 14, 10, 8, 6$. This particular choice is determined by the attempt to minimize the number of coincident discontinuity lines corresponding to different values of K . Indeed, with this choice we have only two jumps of



(c)



(d)

Figure 10. (Continued)

the case $K = 17$ coinciding with two jumps of the case $K = 37$. However, we cannot say that this criterion is the best one in all practical cases; the choice of the values of K may depend on the object to be observed.

Since we are mainly interested in verifying that the procedure is capable of reducing the observed artifacts, we do not add noise to the computed chopped and noded images. Moreover, we use the criterion (35) for stopping the iterations, with a suitable value of ε assuring that the asymptotic value of the restoration error has been reached. In particular, we use $\varepsilon = 0.1\%$ in the case of the example (a.1) of figure 2 and $\varepsilon = 0.5\%$ in the case of the example (a.2) of the same figure, while we use $\varepsilon = 3\%$ for the 2D examples. The results obtained are reported in tables 1–4 where k_0 is the number of iterations defined by conditions (35) and ϱ_0 is the corresponding restoration error on the observation region, i.e. $\varrho_0 = \varrho_{\text{OR}}^{(k_0)}$.

We observe that the 2D examples exhibit a regular behaviour which does not hold in the 1D examples: when K increases, the restoration error decreases as well as the required number of iterations.

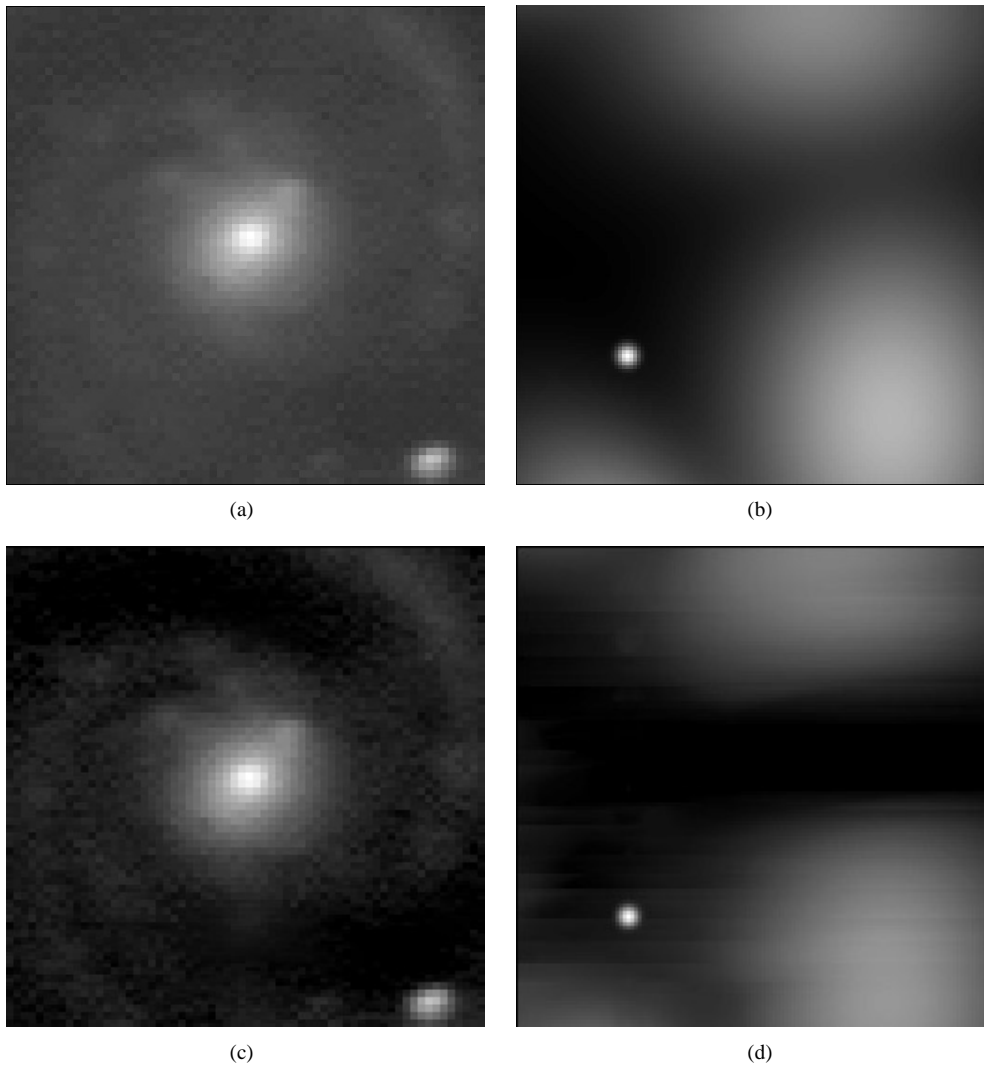


Figure 11. (a) The object of figure 3(a) restricted to the observation region; (b) the object of figure 3(b) also restricted to the observation region; (c) the restoration of (a) as provided by the arithmetic mean of the restorations corresponding to $K = 17, 23, 29, 37$; (d) analogous restoration of (b).

We can apply the procedure suggested at the beginning of this section: for each one of the examples considered we take the arithmetic mean of the four restorations corresponding to the four values of the chopping amplitude. The corresponding restoration errors for the four examples, which must be compared with those reported in tables 1–4, are 8%, 5.6%, 5.1% and 23.3%. As we can see, these errors, in general, are not smaller than the smallest restoration error reported in these tables. However, the restorations obtained by means of the averaging procedure are qualitatively better than those obtained by a single value of K . This effect is evident in figure 10, which refers to the 1D examples, and can also be verified for the 2D examples by comparing figure 11 with figure 8.

where ω is a parameter to be determined. Then from equation (B1) we get

$$1 - 2e^{iK\omega} + e^{i2K\omega} = (1 - e^{iK\omega})^2 = 0 \quad (\text{B3})$$

i.e.

$$e^{iK\omega} = 1. \quad (\text{B4})$$

This condition provides the following values of ω :

$$\omega_{\pm k} = \pm 2\pi \frac{k}{K} \quad k = 0, 1, \dots, (K - 1). \quad (\text{B5})$$

For fixed k , ω_k and ω_{-k} correspond, in general, to linearly independent vectors. However, from the relation

$$\exp\left(\pm i \frac{2\pi}{K}(K - k)n\right) = \exp\left(\mp i \frac{2\pi}{K}kn\right) \quad (\text{B6})$$

it follows that k and $K - k$ provide the same pair of linearly independent vectors.

Since $k = 0$ provides only one vector, we have the following situation: if K is *odd*, we obtain linearly independent pairs for $k = 1, \dots, (K - 1)/2$ (including the vector corresponding to $k = 0$, we get K linearly independent vectors); if K is *even*, we obtain linearly independent pairs for $k = 1, \dots, (K - 2)/2$ and an additional vector corresponding to $k = K/2$ (again, including the case $k = 0$, we get K linearly independent vectors).

Another set of K linearly independent vectors is obtained if we look for vectors given by

$$(\mathbf{q})_n = n e^{i\omega n} \quad n = 1, \dots, N + 2K. \quad (\text{B7})$$

From equation (B1) we obtain the condition

$$n(1 - e^{i\omega K})^2 = 0 \quad n = 1, \dots, N + 2K \quad (\text{B8})$$

so that we re-obtain the values of ω given by equation (B5). The previous discussion can be repeated and the relationship between a vector \mathbf{p} and the corresponding vector \mathbf{q} is simply given by $q_n = np_n$ ($n = 1, 2, \dots, N + 2K$).

The basis above is not orthogonal; we can derive an alternative basis by making use of theorem 2.1 again. The equation $\mathbf{A}\mathbf{v} = \mathbf{0}$ is in fact equivalent to

$$\bar{\mathbf{T}}\mathbf{u} = \mathbf{0} \quad \text{with } \mathbf{v} = \mathbf{\Pi}_{N+2K}\mathbf{u}. \quad (\text{B9})$$

In the light of the block diagonal structure of $\bar{\mathbf{T}}$, we are able to collect $2K$ orthogonal vectors \mathbf{u} expressed in terms of appropriate elements of the kernel of each block \mathbf{T}_q or \mathbf{T}_{q+1} . We obtain the following orthogonal span for $N(\mathbf{A})$:

$$N(\mathbf{A}) = \langle \mathbf{v}_1^c, \dots, \mathbf{v}_K^c; \mathbf{v}_1^1, \dots, \mathbf{v}_K^1 \rangle \quad (\text{B10})$$

$$(\mathbf{v}_k^c)_n = \begin{cases} 1 & \text{if } n \equiv k \pmod{K} \\ 0 & \text{otherwise} \end{cases} \quad (\text{B11})$$

$$(\mathbf{v}_k^1)_n = \begin{cases} m - 2n + 3 & \text{if } n \equiv k \pmod{K} \\ 0 & \text{otherwise} \end{cases} \quad (\text{B12})$$

where

$$m = \begin{cases} q + 1 & \text{for } k \leq K_1 \\ q & \text{for } k > K_1. \end{cases}$$

It is worth pointing out that the basis $\{\mathbf{p}_k, \mathbf{q}_k\}$ is localized in the frequencies while $\{\mathbf{v}_k^c, \mathbf{v}_k^1\}$ is localized in the space.

Appendix C

In this appendix we give the expression of the matrix $\mathbf{A}^T\mathbf{A}$ to be used in the implementation of the projected Landweber method. One must consider four cases separately: $N \geq 2K$, $2K > N > K$, $N = K$, $N < K$. We give the last two cases only for completeness because, in general, the chopping amplitude satisfies the condition $K < N$.

The results can be easily obtained by computing first $\mathbf{A}^T\mathbf{g}$ for the various cases and then putting $\mathbf{g} = \mathbf{A}\mathbf{f}$.

(i) $N \geq 2K$

$$\begin{aligned} (\mathbf{A}^T\mathbf{A}\mathbf{f})_n &= f_n - 2f_{n+K} + f_{n+2K} & n = 1, \dots, K \\ &= -2f_{n-K} + 5f_n - 4f_{n+K} + f_{n+2K} & n = K+1, \dots, 2K \\ &= f_{n-2K} - 4f_{n-K} + 6f_n - 4f_{n+K} + f_{n+2K} & n = 2K+1, \dots, N \\ &= f_{n-2K} - 4f_{n-K} + 5f_n - 2f_{n+K} & n = N+1, \dots, N+K \\ &= f_{n-2K} - 2f_{n-K} + f_n & n = N+K+1, \dots, N+2K. \end{aligned} \quad (\text{C1})$$

The total number of operations (additions and multiplications) for computing $\mathbf{A}^T\mathbf{A}\mathbf{f}$ is $5N+4K$.

(ii) $2K > N > K$

$$\begin{aligned} (\mathbf{A}^T\mathbf{A}\mathbf{f})_n &= f_n - 2f_{n+K} + f_{n+2K} & n = 1, \dots, K \\ &= -2f_{n-K} + 5f_n - 4f_{n+K} + f_{n+2K} & n = K+1, \dots, N \\ &= -2f_{n-K} + 4f_n - 2f_{n+K} & n = N+1, \dots, 2K \\ &= f_{n-2K} - 4f_{n-K} + 5f_n - 2f_{n+K} & n = 2K+1, \dots, K+N \\ &= f_{n-2K} - 2f_{n-K} + f_n & n = K+N+1, \dots, N+2K. \end{aligned} \quad (\text{C2})$$

The total number of operations is now $5N+6K$.

(iii) $N = K$

$$\begin{aligned} (\mathbf{A}^T\mathbf{A}\mathbf{f})_n &= f_n - 2f_{n+N} + f_{n+2N} & n = 1, \dots, N \\ &= -2f_{n-N} + 4f_n - 2f_{n+N} & n = N+1, \dots, 2N \\ &= f_{n-2N} - 2f_{n-N} + f_n & n = 2N+1, \dots, 3N. \end{aligned} \quad (\text{C3})$$

The total number of operations is $9N$.

(iv) $N < K$

$$\begin{aligned} (\mathbf{A}^T\mathbf{A}\mathbf{f})_n &= f_n - 2f_{n+K} + f_{n+2K} & n = 1, \dots, N \\ &= 0 & n = N+1, \dots, K \\ &= -2f_{n-K} + 4f_n - 2f_{n+K} & n = K+1, \dots, K+N \\ &= 0 & n = K+N+1, \dots, 2K \\ &= f_{n-2K} - 2f_{n-K} + f_n & n = 2K+1, \dots, N+2K. \end{aligned} \quad (\text{C4})$$

The total number of operations is $9N$.

References

- [1] Beckers J M 1994 Imaging with array detectors using chopping and other forms of differential detection *Instrumentation in Astronomy VIII (Proc. SPIE vol 2198)* ed D L Crawford and E R Craine, pp 1432–7
- [2] Käuffel H U 1995 Observing extended objects with chopping restrictions on 8 m class telescopes in the thermal infrared *Calibrating and understanding HST and ESO instruments (ESO Conference and Workshop Proceedings vol 53)* ed P Benvenuti, pp 159–63
- [3] Golub G H and van Loan C F 1983 *Matrix Computations* (Baltimore, MD: Johns Hopkins University Press)

- [4] Serra S 1998 On the extreme eigenvalues of Hermitian (block) Toeplitz matrices *Linear Algebra Appl.* **270** 109–29
- [5] Robberto M and Herbst T M 1998 MAX: the new MPA thermal infrared imager *Infrared Astronomical Instrumentation (Proc SPIE vol 3354)* ed A M Fowler, pp 711–19
- [6] Bertero M, Boccacci P and Robberto M 1998 An inversion method for the restoration of chopped and nodded images *Infrared Astronomical Instrumentation (Proc SPIE vol 3354)* ed A M Fowler, pp 877–86
- [7] Bertero M and Boccacci P 1998 *Introduction to Inverse Problems in Imaging* (Bristol: Institute Of Physics)
- [8] Eicke B 1992 Iteration methods for convexly constrained ill-posed problems in Hilbert space *Num. Funct. Anal. Opt.* **13** 413–29
- [9] Engl H W, Hanke M and Neubauer A 1996 *Regularization of Inverse Problems* (Dordrecht: Kluwer)